A Simulation Tool for Accurate and Fast Assessment of Harmonic Propagation in Modern Residential Grids

Sergey Yanchenko, Flavio B. Costa, and Kai Strunz

***Abstract*—A simulation tool for modeling harmonic propagation in low voltage distribution networks with manifold nonlinear equipment is developed. The tool is based on a hybrid domain approach representing each nonlinear household device with accurate and fast white box model and the supply network – with the harmonic admittance matrix in the frequency domain. Proposed tool features significant reduction of simulation time compared with the brute force time domain (BFTD) simulation, high level of accuracy as opposed to the traditional frequency domain methods, and improved convergence under weak grid conditions in respect to conventional iterative harmonic analysis. Eventually this preconditions the use of the proposed approach in computationally intensive simulations, e.g. in stochastic harmonic modeling with the Monte Carlo method. Additionally two application examples of the developed tool are provided demonstrating its effectiveness compared to the BFTD modeling.**

***Index Terms*—Harmonic analysis, power quality, power system harmonics.**

I. Introduction

NONLINEAR household appliances increase their share in total energy consumption of low voltage (LV) residential networks with the rapid development of semiconductor technology and penetration of renewable energy systems. As a result, under cumulative effects of multiple appliances operating simultaneously within the network, voltage and current harmonics can reach significant levels. In order to avoid potential risks for the reliable system operation and to assess various grid operating modes, realistic studies of harmonic impacts and propagation within large distribution networks need to be performed [1]–[4]. The task of network harmonic analysis can be generally addressed by frequency domain (FD), time domain (TD) or hybrid domain (HYD) approaches [5]–[10].

The FD approach implies building a linear matrix equation, interrelating harmonic nodal voltages and harmonic current injections of nonlinear loads by network admittance matrix for each frequency of interest [5], [6]. The resulting linear representation of harmonic propagation introduces significant simplifications into the simulation process by neglecting mutual interaction between supply voltage and device current harmonics, thus sacrificing the modeling accuracy for the sake of computational speed [8]. This drawback can be alleviated by Norton models that represent each nonlinear load with harmonic current source and frequency admittance matrix [11]. However, due to the black-box nature of the model its ability to represent multiple devices with varying parameters is significantly limited.

The TD approach provides a periodic steady-state solution of a state-space system representation [7], [8]. The sequential integration of system ordinary differential equations (ODEs) until the steady state provides an accurate solution. However, this may require considerable time and computing resources for the systems with light damping and eventually limits the use of the BFTD approach for relatively simple simulations only [10]. Time variations of harmonic levels can be also acquired by Harmonic State Space approach [12] that provides accurate transient representation for multiple harmonic orders but is computationally intensive and, hence, slow.

The HYD approach satisfies the controversial requirement for fast computation and realistic representation of harmonic behavior. The account for complex interactions within modern electronic equipment that is inevitable for accurate harmonic model results in significant computational burden if the detailed models are multiplied for the use in large-scale simulations. The HYD approach combines the accuracy of TD models of nonlinear loads with the computational speed of FD calculations of harmonic grid propagation [9], [10]. According to the HYD approach, the modeled network is divided into: 1) linear part, containing grid impedance and feeding cables and effectively simulated in the FD; 2) nonlinear part, including residential loads that can be accurately modeled by means of suitable white-box models. Potential cable related harmonic resonances are neglected assuming relatively low distances inherent for residential networks. The steady state harmonic levels are determined in the course of iterative procedure generally referred to as iterative harmonic analysis (IHA) [6]. This approach provides significant

Manuscript received March 25, 2020; revised July 17, 2020; accepted August 19, 2020. Date of publication September 1, 2020; date of current version July 23, 2021. This work was supported by the research Grant #8.8463.2017/BCh of Russian Ministry of Science and Education and project STR 1437/1-1 within priority program 1984 by DFG of Germany. Paper no. TPWRD-00444-2020. *(Corresponding author: Sergey Yanchenko.)*

Sergey Yanchenko is with the Department of Electric Supply of Industrial Enterprises, Moscow Power Engineering Institute, Moscow 111250, Russia (e-mail: yanchenkosa@mpei.ru).

Flavio B. Costa is with the School of Science and Technology (EC&T), Federal University of Rio Grande do Norte, Natal 1524, Brazil (e-mail: flaviocosta@ect.ufrn.br).

Kai Strunz is with the Department of Sustainable Electric Networks and Sources of Energy, Technische Universität Berlin, Berlin D-10587, Germany (e-mail: kai.strunz@tu-berlin.de).

Color versions of one or more of the figures in this article are available online at https://ieeexplore.ieee.org.

Digital Object Identifier 10.1109/TPWRD.2020.3020754

reduction of calculation time, however may suffer from the convergence issues under weak grid conditions or resonances [13]. To improve convergence, Newton iterative procedure is used together with harmonic sensitivity matrices of nonlinear loads [14]. However, the calculation of these matrices presents a certain complexity and is not suitable for large-scale harmonic analysis.

Despite of these recent developments, commercial software as well as harmonic penetration studies [15], [16] still utilize the simplest and the fastest FD current source approach as the main methodology for network harmonic simulations. This is computationally effective but leads to significant overestimation of distortion levels. Conversely, the use of HYD methods is usually limited to the cases of single nonlinear loads or low impedance networks due to the convergence problems and the complex derivation of harmonic sensitivity matrices.

This paper proposes a simulation tool for network harmonic analysis capable of realistic modeling of large amounts of residential loads and at the same time featuring improved convergence under high impedance or resonant network conditions. Based on the HYD approach the improvement of presently adopted harmonic propagation analyses is accomplished by: 1) developing accelerated individual white-box harmonic models for major types of household equipment; 2) proposing convergence improvement of IHA procedure achieved by simplified determination of harmonic sensitivity matrices.

The acquired experience of applying acceleration techniques for particular topologies of household equipment allows to define the most accurate and computationally effective solution methods for the particular types of nonlinear devices. Additionally the capability of the simulation tool to handle resonant and high impedance conditions removes the present limitations of IHA in respect to the grids with high impedance values.

Eventually, the diverse types of considered devices, ease of adding models of newer types of equipment to the simulation, capability to account for manifolds of devices within households, and improved method convergence guarantee a realistic and up-to-date representation of harmonic levels in permanently developing LV residential grids. This makes the proposed simulation tool potentially implementable into harmonic impedance studies, including harmonic resonance assessment or filter design; estimation of harmonic induced effects like additional losses in cables and transformers; and stochastic modeling of random harmonic levels based on e.g. Monte Carlo Markov Chain approach.

This paper consists of two parts in accordance with the main stages of HYD approach. The first part introduces the accelerated ODE representations of previously developed models of typical equipment including traditional harmonic sources like compact fluorescent lamps (CFL) and switch mode power supplies (SMPS) and modern converters like inverters for the renewables. The quality of the modeling is illustrated by comparison with the measured data of commercially available equipment. The second part describes adoption of techniques for improved convergence and the implementation of accelerated ODE models into IHA in order to produce a tool for simulating network harmonic propagation. Additionally, a brief demonstration of the use of suggested simulation tool for determining harmonic distribution along the network and determination of the network impedance is provided.

Matlab was used as an environment for development of the simulation tool while its main blocks including accelerated models of devices, various modules of IHA were implemented as respective functions. Likewise, Simulink was used to acquire the BFTD solution that was further employed as a reference in the justification of the accuracy and effectiveness of the models. Despite of the variety of currently available software tools for TD simulations, this choice is justified by significant speed-up (10–50 times) provided by accelerated models. The achieved acceleration is high enough to be able to generalize the results for other time-domain simulation software featuring individual levels of computational efficiency compared to Simulink.

II. Adopted Modeling of Household Devices

The use of regular BFTD approach for simulating manifold nonlinear devices connected to LV residential networks within the framework of IHA turns out to be time-consuming and ineffective. Particularly, more appropriate harmonic models of household equipment should be developed, featuring accurate representation of the steady-state current waveform and at the same time significant acceleration of simulation process compared to BFTD approach.

In order to satisfy these requirements, three modelling methods were adopted in this paper, namely Limit Cycle Time Domain approach (LCTD) [10], Trapezoidal Method of Integration (TMI) [17], and Harmonic Domain (HD) method [18]. Previously developed models of household equipment [20]–[24] were represented as ODE systems of the standard form:

$$\mathbf{x}'(t) = f(\mathbf{x}(t), \mathbf{u}(t)), \tag{1}$$

where $\mathbf{x}(t)$ and $\mathbf{u}(t)$ – state variable and input vectors for the n-phase system, respectively.

Equation (1) can be linearized around the steady state $\mathbf{x_0}(t)$ by Taylor series containing first-order partial derivatives:

$$f(\mathbf{x}(t)) \approx f(\mathbf{x}_0(t)) + \sum_i \partial f(x_i(t),u(t))/\partial x_i(t) \cdot \Delta x_i(t); \tag{2}$$

and eventually (1) can be linearized to the state-space form:

$$\mathbf{x}'(t) = \mathbf{A} \cdot \mathbf{x}(t) + \mathbf{B} \cdot \mathbf{u}(t), \tag{3}$$

where $\mathbf{A}$ – state matrix and $\mathbf{B}$ – input matrix;

The ODE system (1) were used as an input for one of the three adopted harmonic modeling approaches in order to acquire improved harmonic models in the form of Matlab functions suitable for use in network simulations. Hereafter, a brief description of each of the modeling methods is provided, whereas a comprehensive theoretical background of these methods can be found in corresponding references.

A. Limit Cycle Time Domain Approach

The main idea of the LCTD method [10] is to determine the initial conditions of the ODE system corresponding to its limit

cycle, i.e. steady state, and thus skip the starting transient of the ODE system. The estimate of a limit cycle can be derived iteratively as a result of the Newton process in accordance to

$$\mathbf{x}^{\infty} = \mathbf{x}^{i} + \left(\mathbf{I} - \mathbf{B_0}\right)^{-1} \cdot \left(\mathbf{x}^{i+1} - \mathbf{x}^{i}\right), \tag{4}$$

where $\mathbf{x}^{\infty}$ - a state variable vector at the steady state; $\mathbf{x}^{i}$, $\mathbf{x}^{i+1}$ – values of a state variable vector at t and $t + T$, corresponding to the i^{th} and $(i+1)^{\text{th}}$ iteration steps; T – period; $\mathbf{I}$ – identity matrix; $\mathbf{B_0}$ – state transition matrix, determined numerically as a finite-difference derivative [10].

B. Trapezoidal Method of Integration

According to TMI [17] a standard continuous ODE system (3) allows a discrete representation as follows:

$$\mathbf{x}\left(t\right) = \mathbf{M} \cdot \mathbf{x}(t - \Delta t) + \mathbf{N} \cdot \left(\mathbf{u}(t - \Delta t) + \mathbf{u}\left(t\right)\right) \tag{5}$$

where $\mathbf{M}$ and $\mathbf{N}$ – matrices defined by $\mathbf{A}$ and $\mathbf{B}$ under the assumption of trapezoidal approximation [17].

In case of circuits with switchings equation (3) can be produced individually for each switching state of the system. Consequently, the derivation of the steady-state solution of (1) will consist in accurate determination of the time instants corresponding to the switchings of the system. This can be effectively done by sweeping the values of the switching instants along the expected interval and calculating (3) until the convergence criteria is accomplished.

C. Harmonic Domain Approach

Harmonic domain approach [18] implies transforming linear TD n-phase periodic system of (3) into linear time invariant FD system of harmonic order h:

$$\mathbf{D_{Dh}} \cdot \mathbf{X} = \mathbf{A_e} \cdot \mathbf{X} + \mathbf{B_e} \cdot \mathbf{U}, \tag{6}$$

where $\mathbf{X}$ and $\mathbf{U}$ – Fourier transforms of state variable and input signal vectors of size $n{\cdot}h$ x 1; $\mathbf{A_e}$ and $\mathbf{B_e}$ – coefficient matrices of state variable $\mathbf{X}$ and input signal $\mathbf{U}$ vectors; $\mathbf{D_{Dh}}$ – differentiation diagonal $n{\cdot}h$ x $n{\cdot}h$ matrix containing n blocks of diagonal h x h matrices:

$$\mathbf{D_{Dh}} = \text{blkdiag} \left[\text{diag}\left(.., -j\omega, 0, j\omega, ..\right), \ldots, \text{diag}\left(.., -j\omega, 0, j\omega, ..\right)\right] \tag{7}$$

The terms of (6) are rearranged in order to acquire the form more suitable for Newton procedure:

$$\mathbf{F} = \left(\mathbf{D_{Dh}} - \mathbf{A_e}\right) \cdot \mathbf{X} - \mathbf{B_e} \cdot \mathbf{U} = 0, \tag{8}$$

$$\mathbf{X}^{(i+1)} = \mathbf{X}^{(i)} + \mathbf{\Delta X}^{(i+1)} = \mathbf{X}^{(i)} - \left[\partial \mathbf{F} / \partial \mathbf{X}\right]^{-1} \cdot \mathbf{F}^{(i)} = \mathbf{X}^{(i)} - \left(\mathbf{D_{Dh}} - \mathbf{A_d}\right)^{-1} \cdot \mathbf{F^0}, \tag{9}$$

where $\mathbf{F^0}$ is the value of a nh x nh matrix $\mathbf{F}$ corresponding to the initial guess of the steady state of the state variable $\mathbf{X^0}$ vector; $\mathbf{A_d}$ is coefficient matrix containing partial derivatives of $\partial \mathbf{F} / \partial \mathbf{X}$.

Solving (9) iteratively allows to define steady state solution $\mathbf{X}^{\infty}$ representing the Fourier image state variable vector $\mathbf{x}(t)$.

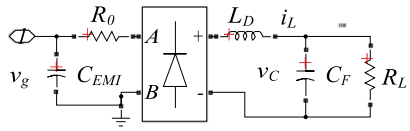

Fig. 1. Simplified circuit of a passive PFC 360 W PC SMPS.

III. Improvement of Previous Harmonic Models of Equipment

The list of devices considered in this paper for harmonic modeling via aforementioned methods is as follows:

1) CFL without power factor correction (PFC) [20];
2) Personal computer (PC) SMPS with passive PFC [20];
3) PC SMPS with active PFC [21];
4) Fridge with single phase induction motor [22];
5) Vacuum cleaner with universal motor [23];
6) Microwave oven (UW) [23];
7) Photo-voltaic (PV) inverters with typical control [24].

Harmonic measurement data of commercially available household devices were acquired from the PANDA Equipment Harmonic Database [19]. General results of harmonic modeling for different devices considered in this section are compared with the measurement data under sinusoidal and distorted supply voltages. For the sake of brevity, models are represented by ODE sets only. Detailed description of original models, circuit operation and accuracy assessment can be found in [20]–[24]. The original circuits were implemented in Simulink whereas those described in this section – as Matlab functions.

A. Rectifier With Passive/Without Power Factor Correction

Fig. 1 presents the simplified circuit of SMPS with passive power factor correction (PPFC), which corresponds to the following ODE system [20]:

State 1 ($v_g > v_C$, $i_L \neq 0$):

$$di_L/dt = 1/L_{DC}(|v_g| - i_L R_0 - v_C); \tag{10}$$

$$dv_C/dt = 1/C_F \left(i_L - v_C/R_L\right). \tag{11}$$

State 2 ($v_g < v_C$, $i_L = 0$):

$$dv_C/dt = -v_C/(C_F R_L). \tag{12}$$

where i_L and v_C – inductor current and capacitor voltage, respectively; L_{DC} – smoothing inductor; R_0 – current limiting resistance; R_L – load resistance; C_F – smoothing capacitance; C_{EMI} – EMI-filter capacitor.

This paper proposes the solution of ODE system (10)–(12) with the TMI instead of the BFTD model in [20]. Comparison with the measured current waveforms for 24 W CFL (Fig. 2) and 360 W PC SMPS (Fig. 3) under sinusoidal and distorted supply voltage justifies good matching capability of the developed TMI model. Table I summarizes the parameter values used for the modeling and shows significant reduction of modeling time compared with [20].

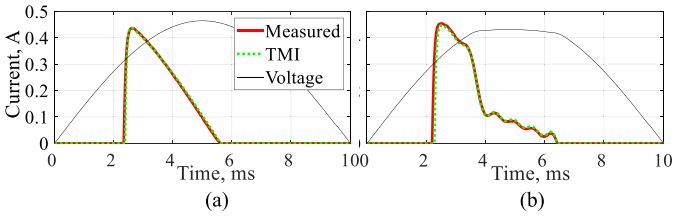

Fig. 2. Measured and modeled current waveforms for 20 W CFL under: (a) sinusoidal supply voltage; (b) distorted supply voltage.

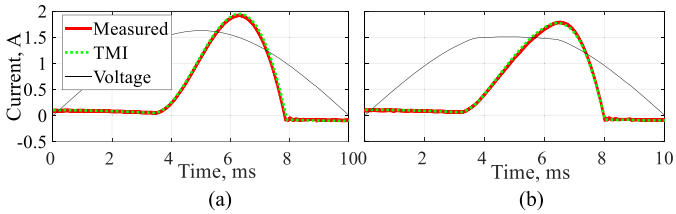

Fig. 3. Measured and modeled current waveforms for 360 W PC SMPS with 150 W load under: (a) sinusoidal supply voltage; (b) distorted supply voltage.

TABLE I
PARAMETERS OF EQUIPMENT WITH DIODE BRIDGE RECTIFIER

Equipment	Power, W	R_0, Ω	C_F, uF	R_L, kΩ	L_{DC}, uH	C_{EMI}, uF	Time, s	
							TMI	[10]
No PFC CFL	24	10	5.8	3. 8	–	–	0.05	0.5
PC with PPFC	150/360	0.1	100	0.58	42	0.5	0.06	0.5

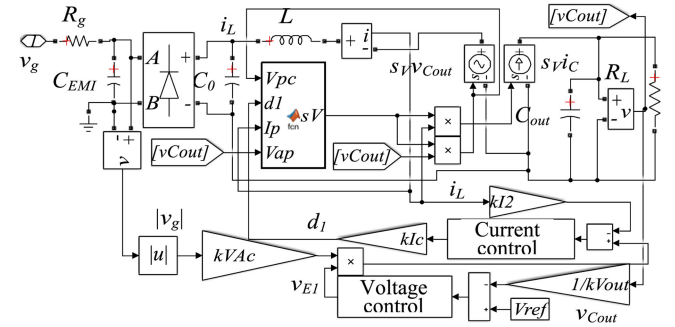

Fig. 4. Simplified circuit of an active PFC PC SMPS.

B. Power Supply With Active Power Factor Correction Circuit

Fig. 4 presents the simplified circuit of SMPS with active PFC which corresponds to the following ODE set [21]:

$$di_L/dt = 1/L\,(v_{C0} - v_{C\text{out}} s_V)\,; \tag{13}$$

$$dv_{C\text{out}}/dt = 1/C_{\text{out}}\,(i_L s_V - v_{C\text{out}}/R_L)\,; \tag{14}$$

$$dv_{E1}/dt = 1/T_{\text{V}}\,(-v_{E1} - k_V/k_{V\text{out}} v_C + k_V V_{\text{ref}})\,; \tag{15}$$

$$dv_{E2}/dt = v_{E1}|v_{\text{g}}|K_{Vac} - k_{I2} i_L; \tag{16}$$

$$d_1 = k_{IC} \cdot (v_{E2} + T_C dv_{E2}/dt)\,; \tag{17}$$

$$d_2 = 2Li_L f/(d_1 v_{C\text{out}} s_V) - d_1; \tag{18}$$

$$ds_V/dt = (d_2/(d_1 + d_2) - s_V) \cdot 10^5; \tag{19}$$

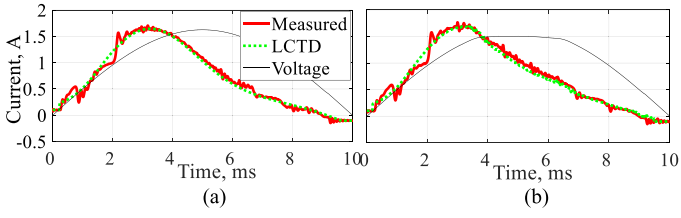

Fig. 5. Measured and modeled current waveforms for 450 W APFC PC SMPS under: (a) sinusoidal supply voltage; (b) distorted supply voltage.

TABLE II
PARAMETERS OF THE 450 W APFC PC MODEL WITH 150 W LOAD

Power plant								Current loop			Voltage loop			Time, s	
R_g, Ω	C_{emi}, uF	C_0,u F	$k_{V\text{out}}$	L, uH	C, uF	R_L, Ω	k_{Vac}	k_{I2}	k_{IC}	T_C, ms	$k_{V\text{out}}$	k_{V1}	T_V, ms	LCTD	[11]
0.1	1	1	160	750	220	865	0.98	0.4	1500	0.1	160	14.6	0.6	0.11	1.1

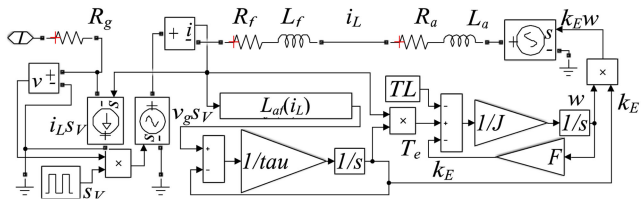

Fig. 6. Simplified circuit of a thyristor-controlled universal motor.

$$dv_{Cemi}/dt = 1/(C_{emi} + C_0)$$
$$[(|v_g| - v_{Cemi})/R_g - i_L sign(v_{Cemi})]; \tag{20}$$

$$dv_{C0}/dt = dv_{Cemi}/dt \cdot sign(v_{Cemi}); \tag{21}$$

where d_1 and d_2 – ON- and OFF-duty cycles of the switch; v_{E1} and v_{E2} – control signals at the outputs of voltage and current control loops; s_V –switching function; L – inductor; C – output capacitor; k_V and T_V – proportional gain and time constant of voltage controller; k_{IC} and T_C – proportional gain and time constant of current controller.

This paper proposes the implementation of ODE system (13)–(21) in accordance with the LCTD approach. Comparison with the measured current waveforms for 450 W active PFC PC SMPS under sinusoidal and distorted supply voltage (Fig. 5) justifies good matching capability of the developed LCTD model. For the sake of simplicity resonant ringing of the measured current (Fig. 5, red line) induced by switch parasitic capacitance is not considered due to negligible effect on total current distortion. A model considering these resonant effects can be found in [21]. The model parameter values are listed in Table II that also demonstrates a speed-up of modeling based on LCTD approach compared with [21].

C. Thyristor-Controlled Universal Motor

Fig. 6 depicts the simplified model of thyristor-controlled universal motor used within vacuum cleaners, electric tools

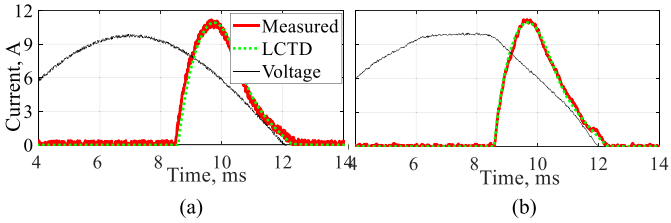

Fig. 7. Measured and modeled current waveforms for 1600 W hoover with 500 W load under: (a) sinusoidal supply voltage; (b) distorted supply voltage.

TABLE III
PARAMETERS OF THE 1.6 kW VACUUM CLEANER MODEL WITH 500 W LOAD

Electrical system					Nonlinear L_{af}			Mechanical system			Switching function			Time, s	
R_a, Ω	L_a, mH	R_f, Ω	L_f, mH	τ, us	p_1 10^{-7}	p_2 10^{-5}	p_3 10^{-3}	$J{\cdot}10^{-6}$, kgm^2	F	T_L, Nm	t_D, s	p_W, %	T_p, ms	LCTD	[13]
0.1	7	0.1	6	20	1.7	-7.1	17	1.3	10^{-5}	0.2	6.55	37	10	0.15	0.7

which corresponds to the following ODE system [23]:

$$di_L/dt = 1/(L_f + L_a)\,(v_g s_V - i_L(R_g + R_a + R_f) - k_E\omega) \tag{22}$$

$$dk_E/dt = 1/\tau\,(L_{af}\,(i_L)\, - k_E) \tag{23}$$

$$L_{af}\,(i_L) = p_1 i^5 + p_2 i^3 + p_3 i \tag{24}$$

$$d\omega/dt = 1/J\,(i_L k_E - T_L - \omega F)\,; \tag{25}$$

where i_L – armature current; R_a, R_f – armature and field winding resistances; L_a, L_f – armature and field winding inductances; L_{af} – nonlinear mutual armature-field inductance; k_E – voltage proportional coefficient; J – mass inertia; T_L – load torque; F – friction factor; p_1, p_2, p_3 – coefficients of the polynomial approximating nonlinear L_{af}.

This paper proposes the implementation of the ODE system (22)–(25) in accordance with the LCTD approach. Comparison with the measured current waveforms for a 1.6 kW vacuum cleaner under sinusoidal and distorted supply voltage (Fig. 7) justifies good matching capability of the developed LCTD model. The model parameters are provided in Table III that clearly shows acceleration achieved by the LCTD approach compared with [23].

D. Capacitor-Run Single-Phase Induction Motor

Fig. 8 presents the model of single-phase induction motor [22]. The corresponding ODE system is based on representation of stator and rotor windings in *dq*-reference frame combined with motion and capacitor shift equations:

$$d\psi_{qs}/dt = \omega \cdot v_g + (\psi_{Mq} - \psi_{qs})\,R_s/L_s; \tag{26}$$

$$d\psi_{qr}/dt = (\psi_{Mq} - \psi_{qr})\,R_r/L_r - \omega_r\psi_{dr}/N_n; \tag{27}$$

$$d\psi_{ds}/dt = \omega v_{ds} + (\psi_{Md} - \psi_{ds})\,R_a/L_a; \tag{28}$$

$$d\psi_{dr}/dt = (\psi_{Md} - \psi_{dr})\,R_r/L_r + N_n\omega_r\psi_{qr}; \tag{29}$$

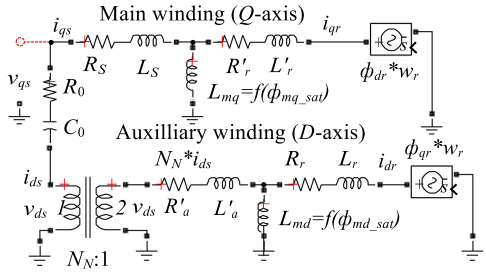

Fig. 8. A model of a capacitor-run single-phase induction motor.

$$\psi_{Mq} = \frac{1}{L_s^{-1} + L_r^{-1} + L_{mq}^{-1}} \cdot \left(\frac{\psi_{qr}}{L_r} + \frac{\psi_{qs}}{L_s} - \frac{\psi_{Mq}}{L_{mq}} \cdot \Delta\psi_{sat}\right); \tag{30}$$

$$\psi_{Md} = \frac{1}{N_n^2 L_s^{-1} + L_r^{-1} + L_{mq}^{-1}} \cdot \left(\frac{\psi_{qr}}{L_r} + \frac{\psi_{qs}}{L_s} - \frac{\psi_{Mq}}{L_{mq}} \cdot \Delta\psi_{sat}\right); \tag{31}$$

$$d\psi_{ds}/dt = \omega v_{ds} + (\psi_{Md} - \psi_{ds})\,R_a/L_a; \tag{32}$$

$$d\psi_{dr}/dt = (\psi_{Md} - \psi_{dr})\,R_r/L_r + N_n\omega_r\psi_{qr}; \tag{33}$$

$$\Delta\psi_{sat} = f(\psi_{Mq}, \psi_{Md}) = (\alpha\sqrt{\psi_{Mq}^2 + \psi_{Md}^2})^{\beta}; \tag{34}$$

$$dv_{ds}/dt = -\omega v'_{\mathrm{g}} - di_{ds}/dt R_0 - i_{ds}/C_0; \tag{35}$$

$$di_{ds}/dt = 1/(\omega L_a)\,(d\psi_{qs}/dt - d\psi_{Md}/dt)\,; \tag{36}$$

$$d\omega_r/dt = p/(J\omega)\,(-T_{L0} + T_{em} - \omega_r F_1)\,; \tag{37}$$

$$T_{em} = -p\,(\psi_{qr} i_{dr} N_n - \psi_{dr} i_{qr}/N_n)\,; \tag{38}$$

$$i_{dr} = 1/(\omega L_r N_n^2)\,(\psi_{dr} - \psi_{Md})\,; \tag{39}$$

$$i_{qr} = 1/(\omega L_r)\,(\psi_{qr} - \psi_{Md})\,. \tag{40}$$

$$\begin{aligned} i_1 &= i_{qs} - i_{ds} \\ &= 1/(\omega L_s)(\psi_{qs} - \psi_{Mq}) - 1/(\omega L_a)\cdot(\psi_{dr} - \psi_{Md}). \end{aligned} \tag{41}$$

where ψ_{qs}, ψ_{ds}, ψ_{dr}, ψ_{qr} – flux linkages related to stator and rotor windings in *dq*-axes; ψ_{Md} and ψ_{Mq} – flux linkages corresponding to magnetizing inductance; $\Delta\psi_{\mathrm{sat}}$ –deviation of the flux linkage from the linear $\psi(i)$ relation as the saturation occurs; α, β –parameters of the saturation curve; i_{qr}, i_{ds}, i_{dr}, - stator and rotor currents in *dq*-axes; v_{ds} – supply voltage of auxiliary winding; T_{em} – electromagnetic torque; ω_r – speed.

This paper proposes implementation of ODE system (26) –(41) in accordance with the HD method. Linearization of (32) representing the saturation of induction motor presents a complicated task as the mutual flux linkages ψ_{Mq} and ψ_{Md} are functions of multiple state variables (equations (30) – (31)) and will produce nonlinear partial derivatives. In order to avoid this, (34) can be rewritten as follows:

$$\begin{aligned} \Delta\psi_{sat} &= \alpha^{\beta}(\psi_{Mq}^2 + \psi_{Md}^2)^{\beta/2} \\ &= \alpha^{\beta}(x_n \cdot x_n + x_{n+1} \cdot x_{n+1})^{\beta/2} = x_{n+2}^{\beta/2}, \end{aligned} \tag{42}$$

TABLE IV
PARAMETERS OF THE 100 W FRIDGE WITH SINGLE-PHASE INDUCTION MOTOR

D-axis			*Q*-axis			Rotor		Satur. curve		Run capacitor		Mechanical system				
L_a, mH	R_a, Ω	L_{Md}, H	L_s, mH	R_s, Ω	L_{Mq}, H	L_r, mH	R_r, Ω	α $\cdot 10^{-3}$	β	C_0, uF	R_0, Ω	T_L, Nm	J, kgm^2	p	N_N	F
11.5	12	2	12.5	3.9	1.9	10.5	11	3.24	47	3.9	2.5	0.65	0.002	2	1.2	0.1

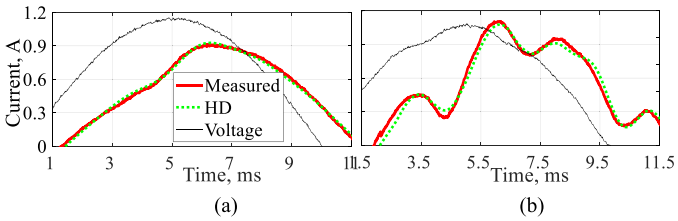

Fig. 9. Measured and modeled current waveforms for 450 W APFC PC SMPS under: (a) sinusoidal supply voltage; (b) distorted supply voltage.

here x_n, x_{n+1} and x_{n+2} are new dummy state variables. Their introduction allows to avoid nonlinearity of partial derivatives in the Taylor series expansion (2) but requires addition of dummy state-space equations of the form (3)

$$dx_n/dt = (\psi_{Md} - x_n) \cdot 10^8; \tag{43}$$

$$dx_{n+1}/dt = (\psi_{Mq} - x_{n+1}) \cdot 10^8; \tag{44}$$

$$dx_{n+2}/dt = \left(x_n^2 + x_{n+1}^2 - x_{n+2}\right) \cdot 10^8; \tag{45}$$

Eventually, (34) is represented in the form of (42)–(45) that is more suitable for linearization and then transformed to (4).

With the parameters provided in Table IV the HD model of single-phase induction motor was compared with the measured current waveforms of 100 W fridge in Fig. 9 that demonstrates the accuracy of the HD approach.

E. PV Inverter With Proportional Integral / Resonant Control

Fig. 10 shows circuits of single-phase PV inverter, PI and PR current controllers, which correspond to the ODE system [24]:

$$C_{DC}dv_{DC}/dt = J_{PV} - i_1 s_V; \tag{46}$$

$$L_1 di_1/dt = v_{DC}s_V - [v_{Cf} + R_C(i_1 - i_2)]; \tag{47}$$

$$(L_2 + L_g)di_2/dt = [v_{Cf} + R_C(i_1 - i_2)] - v_g - i_2 R_2; \tag{48}$$

$$C_f dv_{Cf}/dt = i_1 - i_2; \tag{49}$$

$$di_{ref}/dt = k_{Vi}(V_0 - v_{DC}) - k_{Vp}C_{DC}dv_{DC}/dt; \tag{50}$$

$$dv_{PI}/dt = k_I\left(-i_1 - i_{ref}\sin(\omega t + \alpha)\right)) + \ldots + k_P \left(-i_1 - i_{ref}\sin(\omega t + \alpha) - \omega i_{ref} \cdot \cos(\omega t + \alpha)\right); \tag{51}$$

$$s_V = \left(v_{PI} + v_g\right)/K_{PWM}. \tag{52}$$

$$dv_{PR1}/dt = v_{PR2}; \tag{53}$$

$$dv_{PR2}/dt = -2\omega_b v_{PR2} - \omega_0^2 v_{PR1} + \left(-i_2 - i_{ref}\sin\omega t\right)); \tag{54}$$

$$ds_V/dt = ([2\omega_b k_I v_{PR2} + k_P(-i_2 - i_{ref}\sin\omega t))]/V_0 - s_V) \cdot 10^5. \tag{55}$$

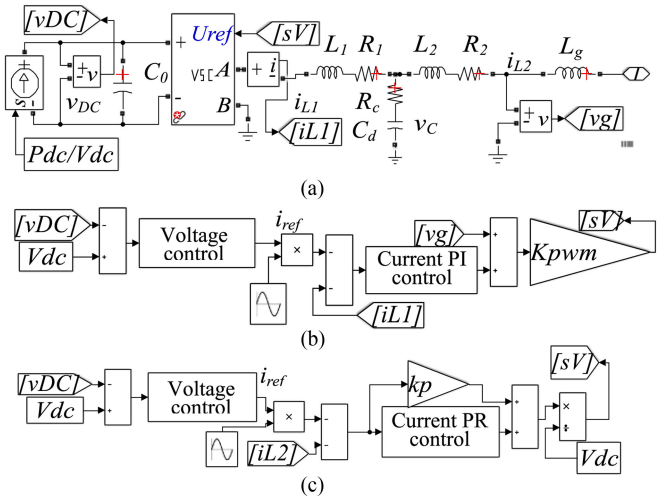

Fig. 10. Simplified circuit of a single-phase PV inverter: power plant (a), PI control loop (b) and PR control loop (c).

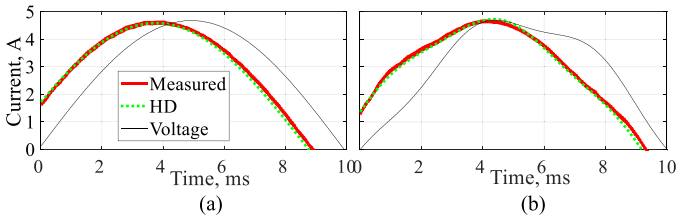

Fig. 11. Measured and modeled current waveforms for 4 kW PV inverter with PI control under: (a) sinusoidal supply voltage; (b) distorted supply voltage.

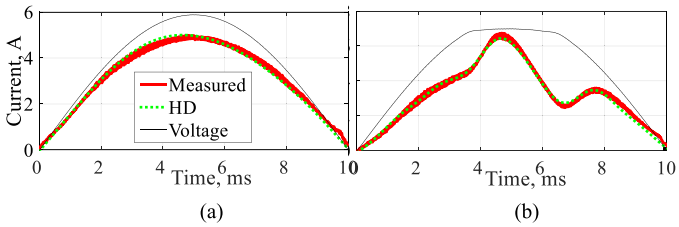

Fig. 12. Measured and modeled current waveforms for 3kW PV inverter with PR control under: (a) sinusoidal supply voltage; (b) distorted supply voltage.

where, v_{DC} – the DC capacitor voltage; i_1 and i_2 – converter- and grid-side currents; v_{Cf} – capacitor voltage of the LCL-filter; i_{ref} – reference current magnitude produced by DC-voltage control loop; v_{PR1} and v_{PR2} – state variables of the PR current controller; v_{PI} – a state variable of PI current controller; s_V – inverter switching function; J_{PV} – PV source output current. This paper proposes implementation of ODE systems of (46)–(55) in accordance with the HD method. The current waveforms of HD models of PV inverters with PI (Fig. 11) and PR control (Fig. 12) were compared with the measurement data of two single-phase PV inverters with 700 W output power, justifying the capability of models to reproduce measurement results. Tables V and VI with model parameter values show reduced simulation times of HD models compared with [24].

TABLE V
PARAMETERS OF THE 4KW PV INVERTER WITH PI CURRENT CONTROL

DC-link		LCL-filter with passive damping								Voltage control		PI current control		Time, s	
V_{DC}, V	C_0, mF	L_1, mH	L_2, mH	R_1, Ω	R_2, Ω	R_d, Ω	C, uF	α,°	P_L, W	K_{Pv}	K_{Iv}, s^{-1}	K_{Pi}	K_{Ii},s^{-1}	HD	[14]
460	15	4.3	1.3	0.1	0.1	4	6	70	700	1.2	11	1.5	1129	0.01	0.55

TABLE VI
PARAMETERS OF THE 4KW PV INVERTER WITH PR CURRENT CONTROL

DC-link		LCL-filter with passive damping							Voltage control		PR current control			Time, s	
V_{DC}, V	C_0, mF	L_1, mH	L_2, mH	R_1, Ω	R_2, Ω	R_d, Ω	C,u F	P_L, W	K_{Pv}	K_{Iv}, s^{-1}	K_{Pi}	K_{Ii},s^{-1}	ω_b, s^{-1}	HD	[14]
750	5	1	.01	0.5	0.1	6	13	750	0.8	11.4	1.9	32	101	0.02	0.5

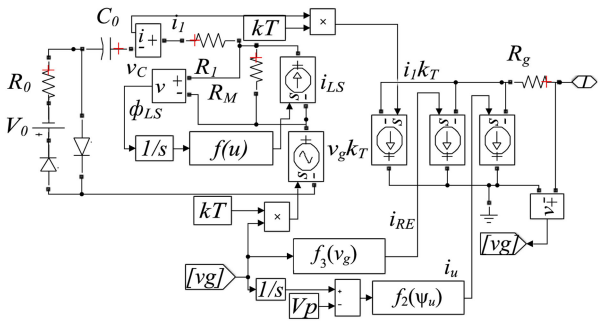

Fig. 13. Simplified circuit of a microwave oven.

F. Microwave Oven

Fig. 13 depicts a simplified model of a microwave oven corresponding to the ODE system written as follows [23]:

State 1. Magnetron irradiation: ($V_2 > V_0$, diode is OFF):

$$dv_C/dt = 1/\left[C_0\left(1+(R_0+R_1)/R_M\right)\right] \left(i_{LS}+(v_g k_T - v_C + V_0)/R_M\right); \tag{56}$$

$$\frac{d\psi_{LS}}{dt} = v_g k_T - \frac{(R_0+R_1)R_M}{R_M+(R_0+R_1)}\left[i_{LS}+\frac{v_g k_T - v_C + V_0}{R_M}\right] - v_C + V_0; \tag{57}$$

$$i_1 = C_0 dv_C/dt; \tag{58}$$

State 2. Capacitor charging ($V_2 < V_0$, diode is ON):

$$dv_C/dt = 1/\left[C_0\left(1+R_0/R_M\right)\right]\left(i_{LS}+(v_g k_T - v_C)/R_M\right); \tag{59}$$

$$d\psi_{LS}/dt = v_g k_T - R_0/(1+R_0/R_M) \cdot\left[i_{LS}+(v_g\cdot k_T - v_C)/R_M\right] - v_C; \tag{60}$$

$$i_1 = C_0 dv_C/dt. \tag{61}$$

Input current of a microwave oven:

$$i_g = i_1 + i_u + i_{RE} \tag{62}$$

$$i_{LS} = f_1(\psi_{LS}) = l_1\psi_{LS}^5 + l_2\psi_{LS}^3 + l_3\psi_{LS}. \tag{63}$$

TABLE VII
PARAMETERS OF A 2KW MICROWAVE OVEN MODEL

Voltage doubler			Magnetron				Leakage inductance			Time, s	
R_0,kΩ	C_0,uF	k_T	R_1,kΩ	V_0,kV	R_M,MΩ		l_1	l_2	l_3	BFTD	[13]
0.47	1.9	8.49	0.3	4	1		0.016	-0.08	0.6	0.15	1.1

TABLE VIII
COEFFICIENTS OF THE POLYNOMIALS REPRESENTING NONLINEARITIES OF A 2KW MICROWAVE OVEN MODEL

Magnetizing inductance								Core loss				
p_1	p_2	p_3	p_4	p_5	p_6	p_7	p_8	r_1	r_2	r_3	r_4	r_5
2.6	25.1	-6.6	-38.9	3.7	17.8	-0.44	-1.9	-1.26	5.6	-8.2	5.4	0.1

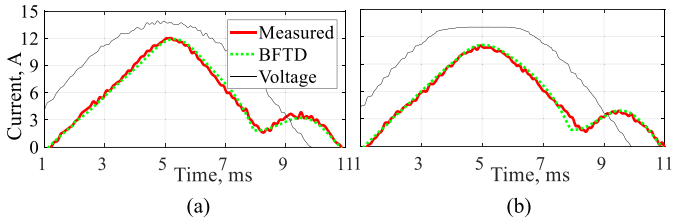

Fig. 14. Measured and modeled current waveforms for 2 kW microwave oven under: (a) sinusoidal supply voltage; (b) distorted supply voltage.

$$i_u = f_2(\psi_u) = p_1\psi_u^8 + p_2\psi_u^7 + \cdots + p_6\psi_u^3 + p_7\psi_u^2 + p_8\psi_u; \tag{64}$$

$$i_{RE} = f_3(v_g) = r_1 \mathrm{v}_\mathrm{g}^7 + r_2 \mathrm{v}_\mathrm{g}^5 + r_3 \mathrm{v}_\mathrm{g}^3 + r_4 \mathrm{v}_\mathrm{g} + r_5. \tag{65}$$

where C_0 and R_0 - parameters of the voltage-doubler circuit, k_T – transformer ratio; V_0 – the lowest voltage required for magnetron irradiation; V_2 – voltage applied to the magnetron; R_1 – equivalent load resistance of a magnetron; f_1, f_2, f_3 – polynomials approximating the respective nonlinearities of leakage and magnetizing inductances and core loss resistance.

This paper proposes the implementation of ODE system (56)–(65) in accordance with TMI approach by representing the nonlinearities with respective partial linear approximations. Based on the parameters of Tables VII and VIII modeling results were compared with the measurement data of the 2 kW microwave oven in Fig. 14. showing good matching capability of the TMI model and increase of computation speed, compared with [23].

G. Discussion of Adopted Modeling Methods

Each of the modeling methods used to speed up calculations has a limited application field defined by the strength of nonlinearity. Depending on the liability of the circuit's nonlinearity to be linearized without significant loss of accuracy, the HD method can be used for slightly nonlinear circuits, the TMI is mostly suited for modeling circuits with switching topologies, while the LCTD effectively handles highly nonlinear circuits. Hereafter, some highlights of the application experience of these models are provided and eventually summed up in the Table IX with the main focus on simulation time. The parameters of the hardware engaged in simulations are as follows: Intel Core i7-HQ CPU with 16 Gb RAM and SATA III SSD.

TABLE IX
SIMULATION TIMES FEATURED BY DIFFERENT TYPES OF MODELS

Model	Type of equipment	Adopted method	Advantages	Limitations	Model time vs Simulink
Bridge rectifier (no PFC)	Energy saving lamps	TMI	High speed; Accuracy	Low efficiency in case of even or inter-harmonics	**0.03s / 0.55s**
Bridge rectifier (PPFC circuit)	Mid power PC SMPSs				**0.06s / 0.6s**
Microwave oven					**0.15s / 1.1s**
PV inverter with PI control	Single phase PV inverters	HD	High speed; Accuracy	Complexity; Low efficiency in case of wide band distortion	**0.01s / 0.55s**
PV inverter with PR control					**0.02s / 0.5s**
Single phase induction motor	Fridges, air conditioners				**0.09s / 1.2s**
Thyristor controlled universal motor	Vacuum cleaners, electric tools	LCTD	Accelerated speed; Accuracy	Complexity	**0.15s / 0.7s**
Active PFC circuit	High power SMPSs				**0.1s / 1.1s**

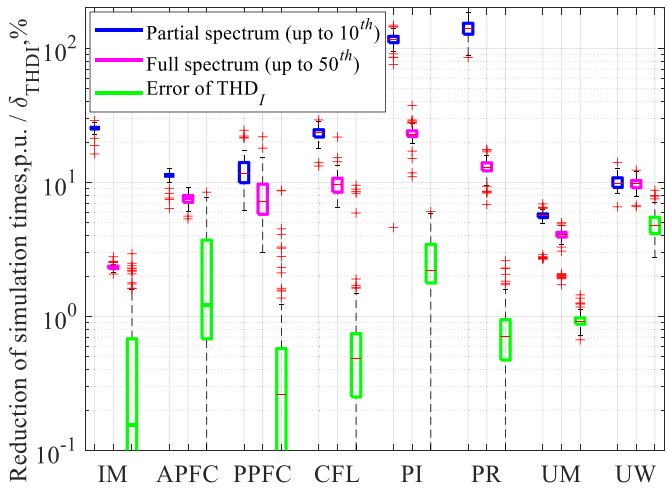

Fig. 15. Reduction of simulation times in respect to Simulink and THDI accuracy of the proposed models.

In order to provide a clearer insight of the modeling process, Fig. 15 depicts the variation of the simulation times and model accuracy acquired from 100 simulations of each device under varying voltage distortion levels. The Simulink discrete stiff solver ode23tb featuring a balance between accuracy and computational speed [25] was adopted for simulations as the most suitable for stiff models containing algebraic loops and complex interactions of variables. The time required by the Simulink model to reach the steady state was determined by the Matlab script controlling the simulation and assessing the difference between the values of 2 consecutive periods of the waveforms.

Depending on the number of considered voltage harmonics the reduction of simulation times of different models is depicted by blue (up to the 10^{th} harmonic) and magenta boxes (up to the 40^{th} harmonic). It follows from the Fig. 15 that the improved models are generally 10–100 faster than their conventional equivalents (blue boxes). Predictably, the increase of considered voltage harmonics slightly dampens this effect (magenta boxes). Finally, the accuracy of accelerated models against conventional brute force approach is verified by presenting the variation of THD_I that does not exceed 5% limit (green boxes, Fig. 15).

Considered devices can be roughly referred to as slightly and highly nonlinear in accordance to the form of the first-order partial derivative (2) resulting from the Taylor series expansion of (1). If $\partial f(x(t))/\partial x_i$ is linear than linearization is accurate and the device is liable for modeling with HD or TMI approach. If $\partial f(x(t))/\partial x_i$ is nonlinear than linearization is inaccurate and LCTD method should be applied.

Slightly nonlinear devices (PV inverters, induction motors, fluorescent lamps with magnetic ballasts) can be modeled with the HD approach. The resulting linearized models (induction motor (IM), PV inverters (PI and PR) in Fig. 15) feature both accurate representation of real nonlinear device ($\delta_{\text{THDI}} \leq 3\%$ – green boxes, Fig. 15) and fast computational speed inherent for a linear circuit (>10 times acceleration – blue boxes, Fig. 15). Nevertheless, the tediousness of defining the coefficient matrices for the cases of large ODE systems results in error-prone procedure that complicates the modeling. Furthermore, wide band voltage distortion and, consequently, a need to model higher harmonic orders, strongly increase the size of the matrix equation (8) thus cancelling out high speed of the HD method (magenta boxes in Fig. 15).

If the nonlinearity of the circuit reveals itself in sequential switchings of linear topologies during the line period (e.g. diode switchings of the bridge rectifier within energy saving lamps or power supplies, voltage doubler circuit of microwave oven), the linearization can be achieved by separately considering each state of the circuit with the TMI. The main benefit of this approach (PPFC, CFL and UW in Fig. 15) is its high speed (>10 times acceleration – blue boxes, Fig. 15) inherent for the analysis of linear circuits and originating from the fact that only half period of the signal is sufficient for accurate current representation ($\delta_{\text{THDI}} \leq 1\%$ for PPFC and CFL– green boxes, Fig. 15) in case of odd harmonics present in the grid. Conversely, if even or interharmonic components need to be considered, then all states of the circuit within one or multiple line periods should be sequentially calculated that significantly degrades the computational performance (magenta boxes, Fig. 15). Devices that can be accurately represented by the TMI include all kinds of passive PFC topologies switching between linear circuits, e.g. capacitor-filtered, capacitor-fed diode bridge rectifiers [20], valley-fill circuit [21], etc.

In case of strong nonlinearities produced by complex relationships of the control system (APFC circuits), linearization approach turns out to be ineffective. Conversely, the LCTD method based on numerical integration of ODEs can be applied (APFC, Fig. 15), that, however, features limited acceleration of computational performance compared with HD and TMI methods (5–10 times acceleration – blue boxes, Fig. 15). Additionally, the solution process within LCTD can be further slowed down in case of stiff ODEs inherent for nonlinear control systems and resulting difficulties in numerical derivation of the state transition matrix $\mathbf{B_0}$ in (1).

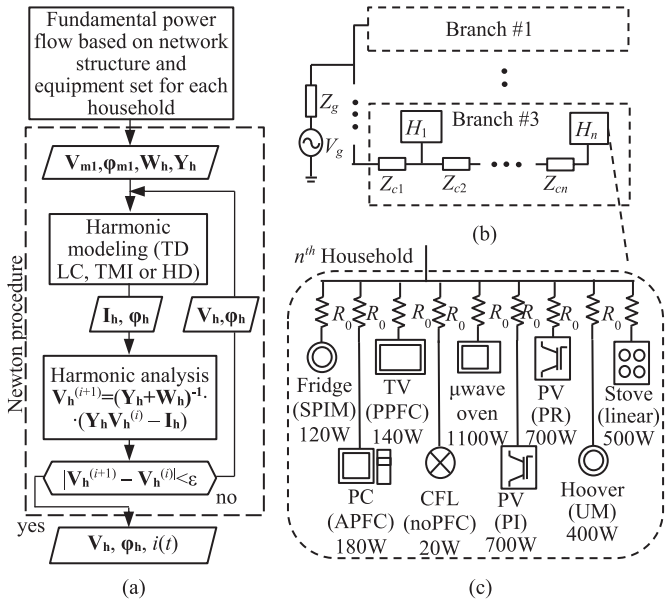

Fig. 16. Modeling methodology: (a) flow chart of implemented IHA, (b) simplified topology of LV network and (c) typical structure of a household.

IV. Harmonic Network Simulations Using Developed Models

The LCTD, TMI and HD approaches adopted in this paper for individual harmonic models in the previous section feature accurate representation of harmonic behavior and at the same time provide significant reduction of simulation time compared to TD methods. Hereafter their implementation in the HYD approach is described as well as proposed improvements of the iterative procedure to strengthen the convergence properties. Eventually, this allows to build up a realistic harmonic analysis tool suitable for accurate and fast modeling of large amounts of household devices in residential LV grids.

A. Adopted Methodology of Network Harmonic Analysis

The flow chart describing the adopted procedure of IHA is depicted in Fig. 16(a) [14]. The input data including the active and reactive power of devices, qualitative set of equipment for each household, grid and branch impedances are uploaded to the standard power flow analysis routine in order to acquire the vectors of steady-state node fundamental voltages $\mathbf{V_m}$ and $\varphi_\mathbf{m}$. The additional output of the power flow analysis is harmonic admittance matrix $\mathbf{Y_h}$. The matrix elements representing connection points of nonlinear loads are updated with the corresponding harmonic admittances of devices, acquired from corresponding harmonic sensitivity matrices $\mathbf{W_h}$. The vectors of fundamental node voltages $\mathbf{V_m}$, $\varphi_\mathbf{m}$ are used as inputs for simulations of all considered devices using the TDLC, TMI or HD models described previously.

The simulation output of each model is used to form a current vector $\mathbf{I_h}$ that is then implemented into Newton-based equation [14] in order to estimate the node harmonic voltages $\mathbf{V_h}$:

$$\mathbf{V_h}^{(i+1)} = (\mathbf{Y_h} + \mathbf{W_h})^{-1}(\mathbf{Y_h}\mathbf{V_h}^{(i)} - \mathbf{I_h}) \tag{66}$$

TABLE X
Parameters of a Simulated Network

Residential grid				Max.number of households with the device, %							
R_g,Ω	L_g,mH	R_C,Ω	R_0,Ω	SPIM	PPFC	noPFC	μwave	PVPI	PVPR	UM	linear
0.05	0.15	0.1	0.1	50	50	50	30	30	30	30	60

Those are again fed to the harmonic models of particular devices, thus closing the iterative loop. The iterations are produced until the difference between sequential iterative node voltages $\mathbf{V_h}^{(i)}$ is less than the specified tolerance ε. The output of the IHA contains the vectors of node harmonic voltages $\mathbf{V_h}$, $\varphi_\mathbf{h}$ and steady-state current waveforms $i(t)$ of each device.

Newton-based equation (60) features better convergence properties than Gauss-Seidel procedure adopted by conventional IHA approach [8]. The improvement is achieved by the use of $\mathbf{W_h}$ matrices representing the sensitivity between different harmonic orders for particular device. In [14] $\mathbf{W_h}$ are determined from the time-domain waveforms for each switching state of considered circuit at each iteration step that can present significant computational burden in case of multiple nonlinear loads. This paper adopts numerical derivation of $\mathbf{W_h}$ constructed of submatrices $\mathbf{W_{ij}}$ that contain the response of the i^{th} current harmonic ΔI_i to the j^{th} voltage harmonic ΔV_j induced as a small voltage stimuli ε_j on the fundamental:

$$\mathbf{W_{ij}} = \begin{bmatrix} \mathrm{Re}\{\Delta I_i(\varepsilon'_j)/\Delta V_j(\varepsilon'_j)\} & -\mathrm{Im}\{\Delta I_i(\varepsilon''_j)/\Delta V_j(\varepsilon''_j)\} \\ \mathrm{Im}\{\Delta I_i(\varepsilon'_i)/\Delta V_j(\varepsilon'_j)\} & \mathrm{Re}\{\Delta I_i(\varepsilon''_i)/\Delta V_j(\varepsilon''_j)\} \end{bmatrix}; \tag{67}$$

here ΔI_i and ΔV_j represent the increment of harmonic current and voltage under sinusoidal ε' and cosinusoidal ε'' j^{th} harmonic stimuli.

B. Validation of the Developed Network Harmonic Model

Fig. 16(b) depicts a simplified three branch LV residential network considered for simulations, that consists of the grid voltage source, network impedance Z_g, branch impedances Z_c of cables feeding the households. Fig. 16(c) shows equipment composition of a standard household corresponding to the list of detailed models. The presence/absence of the device was defined by the uniform random function. Taking into account the crucial role of grid impedance for the performance of IHA approach its values were calculated to represent relatively stiff network based on the following condition:

$$S_{\Sigma\text{load}}/S_{SC} \cdot 100\% \leq 2\% \tag{68}$$

here $S_{\Sigma\text{load}}$ – total load connected to the grid, S_{SC} – grid short circuit capacity. Other parameters of the simulated grid as well as adopted probability values for each equipment are listed in the Table X.

In order to validate the accuracy of the developed approach modeling results for 30 households with randomly varying equipment sets calculated by improved IHA, standard IHA and conventional FD approach were compared with respective output of TD simulation based on models of devices [20]–[24]. The results of 100 simulations for different points along the feeder are depicted in Fig. 17 in the form of error boxplots for low order current and voltage harmonics. First of all significant

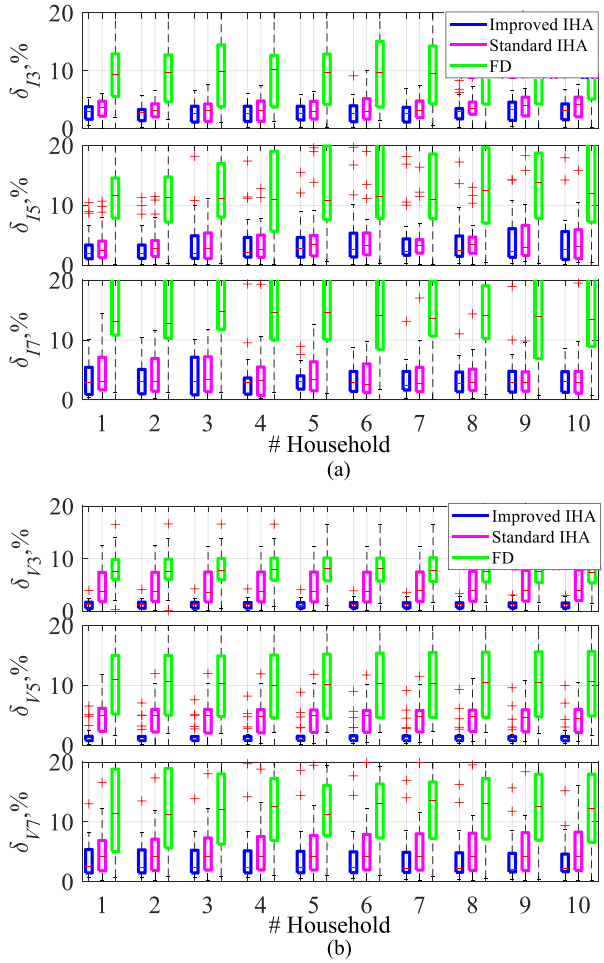

Fig. 17. Accuracy assessment of the results produced by improved IHA, standard IHA, FD and Simulink.

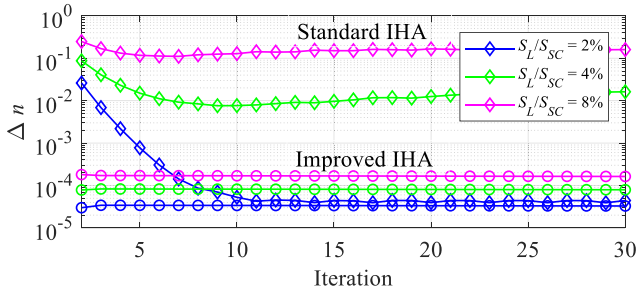

Fig. 18. Convergence of the improved and standard IHA methods under various levels of grid stiffness.

error of simple FD approach (green boxes, Fig. 17) exceeding 10% in most cases can be observed that results from the neglect of harmonic voltage-current interaction of nonlinear loads [20]. Considering the accuracy of the standard IHA method (magenta boxes, Fig. 16) its estimation capability generally deteriorates for the higher harmonic orders and distant points of the feeder with increased grid impedance. The improved IHA approach (blue boxes, Fig. 17) features similar behavior however provides significantly better accuracy in most cases.

Fig. 18 depicts the convergence properties of the improved IHA compared to its conventional version [8] under varying grid

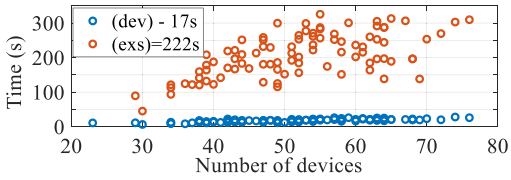

Fig. 19. Comparison of the simulation times produced by improved IHA (dev) and Simulink (exs) for the residential network with 30 households.

impedance conditions. The averaged convergence trajectories for standard (diamond lines) and improved IHA (bubble lines) methods are constructed estimating the norm of the difference of $\mathbf{V_h}$ between successive iterations:

$$\Delta n^{(i+1)} = ||\mathbf{V_h}^{(i+1)} - \mathbf{V_h}^{(i)}|| \tag{69}$$

As expected, convergence of conventional IHA features high sensitivity to the grid stiffness and generally fails even under relatively stiff grid conditions (green line, Fig. 18). Conversely, the improved IHA is much more insensitive to increased grid impedance values that makes it suitable for simulations of resonant conditions.

Finally, Fig. 19 contains the variation of the simulation times required by developed and existing models versus the number of simulated devices. It justifies significant reduction of time produced by IHA network simulation compared to the TD approach.

V. Application Examples of Developed Network Simulation Tool

Hereafter, some application examples of the proposed simulation tool are provided in order to describe its use in typical engineering tasks. The modeling output is validated with the corresponding results of existing models as a reference.

At first, the distribution of harmonic levels along the feeding cable is analyzed. The impact of the cable length between two consecutively connected households on the voltage distortion levels was identified for a cable feeding 20 households with random equipment sets by the developed approach and existing model as a reference. Exemplary the results for the 3rd voltage (green and red lines) and current (deep and light blue lines) harmonics under three levels of active impedance (20 mΩ, 40 mΩ, 80 mΩ) are depicted in Fig. 20(a) showing good matching of developed method with the reference. It follows from the plot that voltage distortion predictably increases for the households most distant from the source. For the higher branch impedance values, higher voltage harmonic levels result in lower current harmonics. Also the cancellation of current harmonic is observed at particular parts of the feeder. Thus, both attenuation and diversity effects [26] are reproduced by the developed tool.

Secondly, the impedance variation of the grid, supplying 30 households, in response to the increasing number of connected PV inverters was estimated by the developed simulation tool. Eventually, impedance magnitude characteristics (Fig. 20(b)) for the cases of 0, 3 and 6 connected PV inverters were built by the developed method (blue squares) with the results of

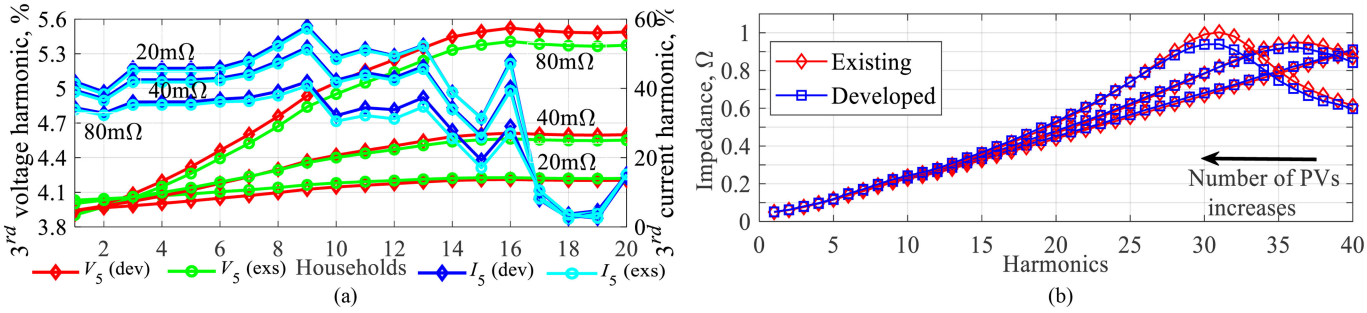

Fig. 20. Application examples of developed tool: (a) - the 3rd harmonic distribution along the feeder of 20 households produced by IHA and Simulink models: voltage (red/green lines) and current (deep/light blue lines) (b) – Network harmonic impedance identification.

existing model as a reference (red diamonds) for the interharmonic multiples of 25 Hz with 50 Hz step in the range of up to 2 kHz. Increasing number of the PV inverters introduces a resonant peak into the grid impedance characteristic due to the significant capacitance associated with inverter LCL-filter. Harmonic impedance produced by developed simulation tool accurately matches the reference even for the cases of hampered convergence under resonance [13].

VI. Conclusion

The proposed approach provides an effective tool for assessment of harmonic propagation in modern residential networks featuring significant reduction of computation time and simultaneously preserving sufficient level of accuracy with the account for voltage-current harmonic interactions. Comprehensive list of considered devices, the correspondence defined between main types of equipment and most suitable acceleration procedures justify the capability of the simulation tool to effectively account for almost any topology of the commercially available devices and easily implement new models of modern equipment. Furthermore, a Newton-based procedure utilizing harmonic sensitivity matrices of particular devices, adopted for harmonic network simulations within the iterative harmonic analysis, guarantees improved convergence of the method even under weak or resonant grid conditions. These benefits allow application of the proposed simulation tool for estimation of harmonic-induced losses, calculation of harmonic effects produced by wide spread of new types of equipment, evaluation of network harmonic impedance, etc.

References

[1] J. Meyer, A. Blanco, and M. Domagk, "Assessment of prevailing harmonic current emission in public low-voltage networks," in *IEEE Trans. Power Del.*, vol. 32, no. 2, pp. 962–970, Apr. 2017.

[2] R. Sinvula, K. M. Abo-Al-Ez, and M. T. Kahn, "Harmonic source detection methods: A systematic literature review," in *IEEE Access*, vol. 7, pp. 74283–74299, 2019.

[3] H. Wang *et al.*, "Modelling of ampacity and temperature of MV cables in presence of harmonic currents due to EVs charging in electrical distribution networks," *IJEPES*, vol. 112, pp. 127–136, 2019.

[4] X. Liang and C. Andalib -Bin- Karim, "Harmonics and mitigation techniques through advanced control in grid-connected renewable energy sources: A review," in *IEEE Trans. Ind. Appl.*, vol. 54, no. 4, pp. 3100–3111, Jul./Aug. 2018.

[5] Task Force on Harmonics Modeling and Simulation "Modeling and simulation of the propagation of harmonics in electric power networks. Part I. Concepts, models, and simulation techniques," in *IEEE Trans. Power Del.*, vol. 11, no. 1, pp. 452–465, Jan. 1996.

[6] J. Arrillaga, *Power System Harmonics*. Hoboken, NJ, USA: John Wiley & Sons, Ltd, 2003.

[7] Task Force on Harmonics Modeling and Simulation. *Tutorial on Harmonics Modeling and Simulation*. IEEE PES, 1998.

[8] A. Medina *et al.*, "Harmonic analysis in frequency and time domain," in *IEEE Trans. Power Del.*, vol. 28, no. 3, pp. 1813–1821, Jul. 2013.

[9] J. d. J. Chavez *et al.*, "Interfacing techniques for time-domain and frequency-domain simulation methods," in *IEEE Trans. Power Del.*, vol. 25, no. 3, pp. 1796–1807, Jul. 2010.

[10] A. Semlyen and A. Medina, "Computation of the periodic steady state in systems with nonlinear components using a hybrid time and frequency domain methodology," in *IEEE Trans. Power Syst.*, vol. 10, no. 3, pp. 1498–1504, Aug. 1995.

[11] A. J. Collin *et al.*, "Analysis of approaches for modeling the low frequency emission of LED lamps," *Energies*, vol. 13, 2020, Art. no. 1571.

[12] J. B. Kwon, X. Wang, F. Blaabjerg, C. L. Bak, and V.-S. Sularea "Harmonic interaction analysis in a grid-connected converter using harmonic state-space (HSS) modelling," *IEEE Trans. Power Electron.*, vol. 32, no. 9, pp. 6823–6835, Sep. 2017.

[13] R. Carbone, M. Fantauzzi, F. Gagliardi, and A. Testa, "Some considerations on the iterative harmonic analysis convergence," in *IEEE Trans. Power Del.*, vol. 8, no. 2, pp. 487–493, Apr. 1993.

[14] J. Usaola and J. G. Mayordomo, "Multifrequency analysis with time-domain simulation," *Euro. Trans. Elect. Power*, vol. 6, pp 53–60, 1996.

[15] G. Ye *et al.*, "Stochastic residential harmonic source modeling for grid impact studies," *Energies* , vol. 10, pp. 372–393, 2017.

[16] D. Salles, C. Jiang, W. Xu, W. Freitas, and H. Erfanian Mazin, "Assessing the collective harmonic impact of modern residential loads—Part I: Methodology," in *IEEE Trans. Power Del.*, vol. 27, no. 4, pp. 1937–1946, Oct. 2012.

[17] N. Mohan, *Power Electronics. Converters, Applications and Design*. Hoboken, NJ, USA: Wiley, 2002, pp. 117–118.

[18] E. Acha, *Power Systems Harmonics: Computer Modeling and Analysis*. Hoboken, NJ, USA: Wiley, 2001, pp. 151–171.

[19] PANDA Equipment Harmonic Database. 2010. [Online]. Available: www.panda.et.tu-dresden.de

[20] A. M. Blanco *et al.* "Impact of supply voltage distortion on the current harmonic emission of non-linear loads," *Dyna*, Aug. 2015, vol. 82, no. 192, pp. 150–159.

[21] S. Yanchenko, and J. Meyer, "Harmonic emission of household devices in presence of typical voltage distortions," in *Proc. Powertech Eindhoven Conf.*, pp. 1–6, Jun. 2015.

[22] S. Yanchenko *et al.*, "Modeling harmonic amplification effects of modern household devices," *Elect. Power Syst. Res.*, vol. 163, pp. 28–37, 2018.

[23] S. Yanchenko, "Harmonic Phenomena of typical low-distortion residential equipment," in *Proc. ICIEAM Conf.*, 2016, pp. 1–6.

[24] S. Yanchenko, and J. Meyer, "Impact of network conditions on the harmonic performance of PV inverters," in *Proc. PSCC Conf.*, 2018, pp. 1–7.

[25] L. Shampine, I. Gladwell, and S. Thompson, *Solving ODEs With MATLAB*. Cambridge, London,UK: Cambridge University Press, 2003.

[26] A. Mansoor *et al.*, "An investigation of harmonics attenuation and diversity among distributed single-phase power electronic loads," in *IEEE Trans. Power Del.*, vol. 10, no. 1, pp. 467–473, Jan. 1995.